International Journal of Biological Macromolecules 148 (2020) 434–448

Contents lists available at ScienceDirect

International Journal of Biological Macromolecules

journal homepage: http://www.elsevier.com/locate/ijbiomac

Fabrication and characterization of dextran/nanocrystalline β-tricalcium phosphate nanocomposite hydrogel scaffolds

Rahil Ghaffari [a], Hamed Salimi-Kenari [a,b,*], Farahnaz Fahimipour [c,e], Sayed Mahmood Rabiee [d], Hassan Adeli [a], Erfan Dashtimoghadam [e]

[a] Faculty of Engineering & Technology, University of Mazandaran, P.O. Box 416, Babolsar, Iran
[b] Department of Chemical and Materials Engineering, New Mexico State University, Las Cruces, NM 88003, USA
[c] Dental Biomaterials Department, School of Dentistry, Tehran University of Medical Sciences, Tehran, Iran
[d] Department of Mechanical Engineering, Babol Noshirvani University of Technology, P.O. Box 484, Babol, Iran
[e] Department of Chemistry, University of North Carolina, Chapel Hill, NC 27599, USA

ARTICLE INFO

Article history:
Received 14 September 2019
Received in revised form 10 January 2020
Accepted 11 January 2020
Available online 15 January 2020

Keywords:
Dextran
Hydrogel
Nanocomposite
β-Tricalcium phosphate
Water uptake mechanism

ABSTRACT

Design of bioactive three-dimensional scaffolds to support bone tissue repair and regeneration become a key area of research in tissue engineering. Herein, porous hybrid hydrogels composed of dextran incorporated with nanocrystalline β-tricalcium phosphate (β-TCP) particles were tailor made as scaffolds for bone tissue engineering. β-TCP was successfully introduced within the dextran networks crosslinked through intermolecular ionic interactions and hydrogen bonding confirmed by FTIR spectroscopy. The effect of β-TCP content on equilibrium water uptake and swelling kinetics of composite hydrogels was investigated. It was found that the homogeneous distribution of β-TCP nanoparticles through the hydrogel matrix contributes to higher porosity and swelling capacity. In depth swelling measurements revealed that while in the early stage of swelling, water diffusion follows the Fick's law, for longer time swelling behavior of hydrogels undergo the second order kinetics. XRD measurements represented the formation of apatite layer on the surface of nanocomposite hydrogels after immersion in the SBF solution, which implies their bioactivity. Cell culture assays confirmed biocompatibility of the developed hybrid hydrogels *in vitro*. The obtained results converge to offer dextran/β-TCP nanocomposite hydrogels as promising scaffolds for bone regeneration applications.

1. Introduction

Applying a temporary and porous three-dimensional (3D) scaffolds for the delivery and integration of cells and/or growth factors at the repair site is one of the most promising strategies for tissue regeneration. The growth of tissues in such substitute is directly affected by microstructure, and bioactivity of the selected materials. Polymeric hydrogels as the crosslinked macromolecular hydrophilic networks capable of retaining high water content and biological fluids are ideal candidates in regeneration medicine [1–3]. The remarkable characteristics of hydrogels, including tunable physio mechanical properties, resemblance to native extracellular matrix (ECM), ability to control the shape, and high porosity allows for cellular proliferation and offer opportunities to overcome tissue vascularization [4–7]. Polysaccharide based hydrogels have emerged as a promising platform for a wide range of tissue engineering applications [8–11]. Among various polysaccharides, dextran, a hydrophilic carbohydrate biopolymer that degrades in certain physical environments without any effect on the cell viability, has been successfully used in tissue engineering applications [12–14]. Dextran is made by bacterial species which consists of (1, 6) α-D-glycoside linkages that each glucose has three hydroxyl groups (OH) in the structure. Dextran hydrogels can provide the excellent condition for cells migration and proliferation. However, the relatively low biological activity of dextran hydrogels restricts their use in hard tissue engineering applications. The bioactivity of dextran hydrogel networks can be improved through incorporation of bioceramics. Nikpour et al., [15] have recently reported nanostructured bioactive glass-dextran composite scaffolds for bone tissue engineering. They have shown that the presence of bioactive glass nanoparticles in the hydrogel matrix not only significantly enhance its mechanical strength, but also improves the reactivity of porous scaffolds to interact with body fluids and produce active sites for mineralization.

β-Tricalcium phosphate (β-TCP) owing to its osteoconduction capability is commonly incorporated into natural polymers to design bone tissue substitute [16–21]. Some studies have reported the application composites consisting of β-tricalcium phosphate with natural polymers

* Corresponding author at: Faculty of Engineering & Technology, University of Mazandaran, P.O. Box 416, Babolsar, Iran.
E-mail address: h.salimi@umz.ac.ir (H. Salimi-Kenari).

https://doi.org/10.1016/j.ijbiomac.2020.01.112
0141-8130/

such as chitosan/gelatin [22], and alginate [8] as the bone tissue substitute. Significantly enhanced new bone formation has been observed using the chitosan composite gel membranes compared with pristine chitosan membranes. Herein, we aim to develop novel dextran/β-TCP composite hydrogels with superior physicomechanical and biological activity characteristics. To the best of our knowledge, dextran composite hydrogels (DCH) comprising tricalcium phosphate have not been reported for tissue engineering applications so far. To this end, the effect of β-TCP content on the microstructure and swelling properties of composite hydrogels is studied.

It is worth to note water uptake capacity is one of the most important features of composite hydrogels, which is essential for their bioactivity and regenerative capacity [23]. Hydrogels swelling plays a critical role in cell migration, proliferation and also facilitates the transport of oxygen and nutrients. Yet, a balance between swelling of nanocomposite hydrogels and other physicomechanical properties should be achieved to offer successful bone tissue regeneration [24]. Hence, to fabricate nanocomposite dextran hydrogel with modulated swelling behavior, assessment of inter and intramolecular interactions between bioceramic nanoparticles and dextran matrix is required.

In the present study, dextran/β-TCP nanocomposite hydrogels (DCH-*x*, which *x* denotes the β-TCP content in *wt%*) are prepared *via* chemical crosslinking and characterized by Fourier transform infrared spectroscopy (FTIR), scanning electron microscopy (SEM), and thermogravimetric analysis (TGA) techniques. Further, the water uptake kinetics of (DCH-*x*) hydrogels in deionized water and simulated body fluid (SBF) are studied. Finally, the bioactivity of DCH-*x* hydrogels is evaluated by immersion in SBF, and their cellular activity is assessed *in vitro*.

2. Materials and methods

2.1. Materials

Dextran (40,000 $g \cdot mol^{-1}$ weight average molecular weight) was purchased from Pharmacosmos A/S, Denmark. Sodium hydroxide, epichlorohydrin (ECH) and β-tricalcium phosphate (β-TCP) powder were purchased from Merck, Germany. Simulated Body Fluid (SBF) was purchased from Pardis Pajhohesh, Yazd, Iran. Chemicals were of analytical grade and used as supplied without further purification. Deionized water (high-performance liquid chromatography grade) was prepared in house using reverse osmosis technique (AquaMax 311, Youngkin Instruments, Anyang, South Korea) and used in this research.

2.2. Synthesis of dextran nanocomposite hydrogels

The crosslinked dextran nanocomposite hydrogels (DCH-*x*) were synthesized based on a method previously reported by Salimi-Kenari et al. [14,15,25–27]. Fig. 1(A, B) shows the steps involved in the fabrication of DCH-*x* hydrogels. Initially, a certain amount of dextran powder was dissolved in 1.8 M sodium hydroxide aqueous solution to prepare the dextran solution (37.5 *w/v%*). In the next step, the different amount of β-TCP (0, 1, 2.5, 5, 10 and 20 *wt%*) was dispersed in the dextran solution. The dextran/β-TCP solutions were stirred under magnetic stirring for 30 min. The resultant solutions were subjected to sonication using an ultrasonic bath for 30 min to improve dispersion of β-TCP in the aqueous solution. Subsequently, a corresponding amount of epichlorohydrin (ECH) 12 *v/v%* as a chemical crosslinking agent was added into

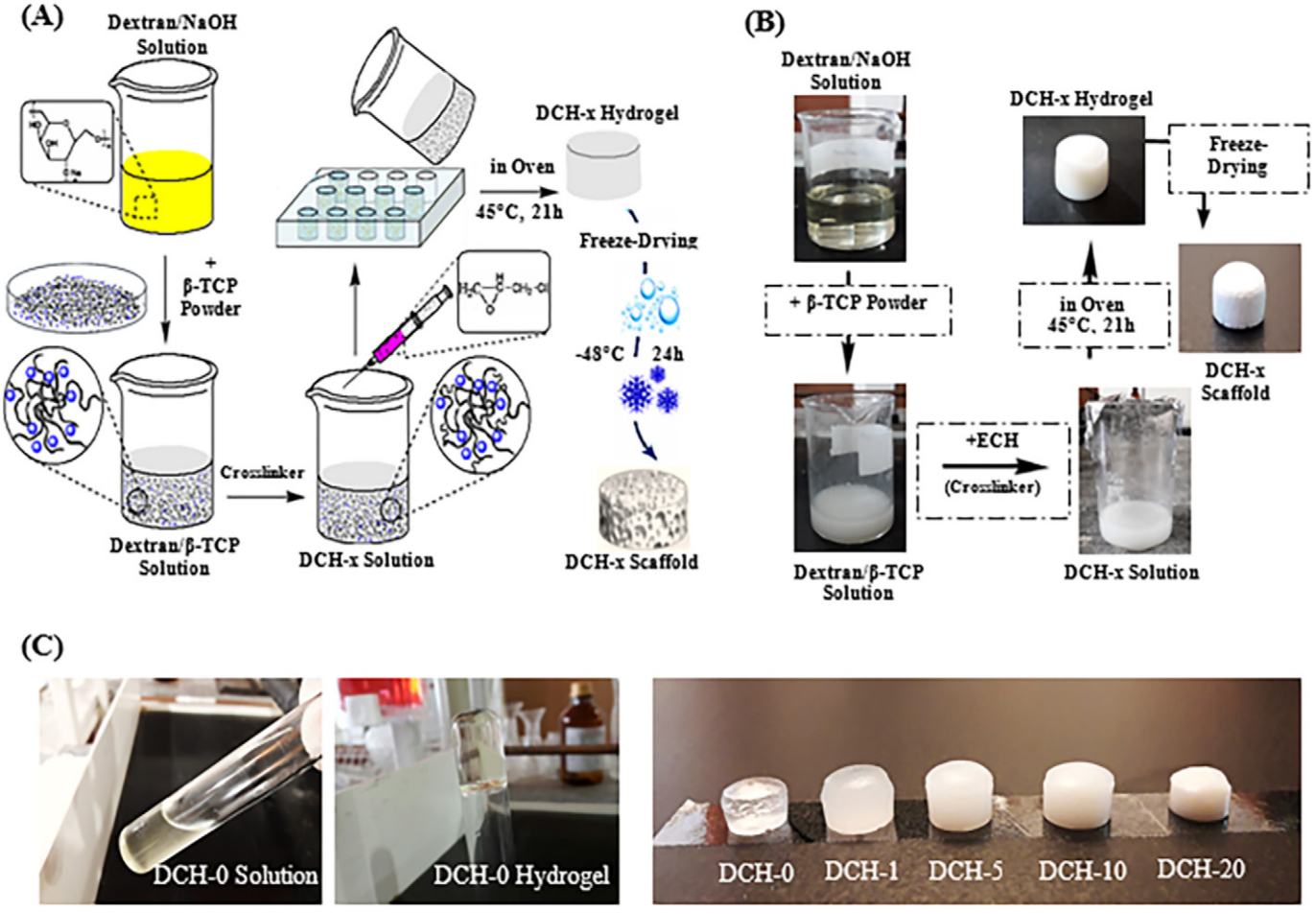

Fig. 1. (A) Schematic illustration of the preparation of dextran/β-TCP nanocomposite hydrogels (DCH-*x*), (B) the visual aspect of the laboratory fabrication of DCH-*x* samples according to preparation procedure in schematic illustration (A), and (C) visual aspect of DCH-*x* samples at the time before and after gelation and final obtained DCH-*x* at different concentrations.

solutions. After 30 s of sonication, the resultant mixtures were poured into the containers and incubated in a convection oven for 21 h at 45 °C to complete the crosslinking reaction. To remove sodium hydroxide and unreacted dextran and ECH, the prepared DCH-*x* nanocomposite hydrogels were washed with distilled water and ethanol. The swollen hydrogels were freeze-dried at −48 °C and stored for further characterization.

2.3. Structural characterizations

2.3.1. Fourier transform infrared spectroscopy (FTIR)

FTIR spectra of β-TCP and DCH-*x* formulations were obtained using an FTIR spectrometer (TENSOR 27, Bruker, Germany) to identify the crosslinked structure and intermolecular interactions between of β-TCP and dextran functional groups in the range from 400 and 4000 cm^{-1} at 4 cm^{-1} resolution and 16 scans. For FTIR analysis, dried β-TCP and freeze-dried hydrogels were thoroughly grounded and mixed with potassium bromide (KBr) at a specific ratio and pressed into pellets for characterization.

2.3.2. X-ray diffraction (XRD)

The crystalline structure of the β-TCP and DCH-*x* samples was analyzed by X-ray diffractometer (PW1730, Philips, Netherlands) (Cu K_α radiation) operating at 40 kV and 40 mA, with a scanning step size of 0.05° at 2θ range 10–60° with a count rate of 1 s per step. The obtained XRD patterns were matched with the JCPDS reference pattern using the X'Pert HighScore software. The average crystals size of β-TCP in the DCH-*x* samples was then calculated *via* Scherrer's equation:

$$D = 0.9\lambda/\beta.\ \cos\theta \quad (1)$$

In this expression, D represents the crystallite size (nm), λ is the X-ray wavelength, θ is the Bragg angle, and β is the line broadening at half the maximum intensity of the selected peaks in the diffractogram.

2.3.3. Scanning electron microscopy (SEM)

Morphology and particle size of β-TCP were acquired using Field Emission Scanning Electron Microscope (FESEM) (Mira, TESCAN, Czech Republic). The average size of the particles was determined by measuring the diameter of at least 50 randomly selected particles using the ImageJ software. The cross-section morphology of DCH-*x* samples was observed using Scanning Electron Microscopy (SEM) (VEGA3, TESCAN, Czech Republic). Prior to SEM, the freeze-dried samples were cross-sectionally cut into thin sections using a razor blade and were coated with a gold layer (*ca.* 60 nm thick). The average pore size of DCH-*x* hydrogels was determined by measuring at least 50 randomly selected pores from different regions of each sample using the ImageJ software. Moreover, energy-dispersive x-ray spectroscopy (EDX) (VEGA3, TESCAN, Czech Republic) was performed to investigate β-TCP distribution.

2.3.4. Thermal analysis

To assess the feasible interactions between dextran chains and β-TCP particles, thermogravimetric analysis (TGA) was carried out using a TGA-PL instrument (Polymer Laboratories, UK) under dynamic air atmosphere at a heating rate of 10 °C·min^{-1} and temperature interval between ambient temperature up to 600 °C.

2.3.5. Porosity measurement

The average porosity of fabricated DCH-*x* samples ($n = 3$) was evaluated using the liquid displacement technique. *n*-Hexane was chosen as the displacement liquid because it can penetrate through the hydrogel network with no shrinkage or swelling of the matrix. Initial weight (W) and volume (V) of the freeze-dried hydrogels were measured and recorded. Samples were then immersed in *n*-hexane overnight and weighed after the excess amount of hexane on the surface was blotted (W'). The porosity of DCH-*x* nanocomposite hydrogels was obtained according to the below equation,

$$\text{Porosity}\ (\%) = [(W\prime - W)/(V \times \rho)] \times 100 \quad (2)$$

where ρ is the density of hexane.

2.3.6. Swelling behavior

The equilibrium swelling ratio (ESR) of the DCH-*x* samples were measured by complete immersion of samples in distilled water and simulated body fluid (SBF) solution at room temperature for three days. The surface water on the nanocomposite hydrogels was blotted using filter paper and then weighed accurately [14,15]. The equilibrium swelling ratio was determined using the following equation:

$$\text{ESR}\ (\%) = (W_\infty - W_0)/W_0 \times 100 \quad (3)$$

where W_∞ and W_0 are the weights of the DCH-*x* samples in the swollen and initial state, respectively.

Swelling kinetics of the hydrogel was measured as follows: an accurately weighed sample (0.2 g) was fully contacted with 300 ml distilled water and SBF solution. At certain time intervals, the swelling capacity of the sample at a given time (W_t, g/g) was measured by weighing the swollen hydrogel and calculated according to Eq. (3). In all cases, five samples were examined and results were reported in average.

2.3.7. Mechanical properties

The mechanical behavior of the composite scaffolds in a swollen state (ESR = 200%) was evaluated in compression mode, according to ASTM F-2150 (Universal Testing Machine Instron, 3382). The cylindrical composite scaffolds measuring 4 mm height and 10 mm diameter were compressed between stainless steel plates using a 50 N load cell at a constant strain rate of 0.1 mm·min^{-1} until failure. Tests were performed with a gauge length of 150 mm. The compressive modulus was determined from the slope of the linear region of the stress-strain curves in the 0–30% strain range. Five replicates per sample were tested.

2.3.8. In vitro cellular activity

The *in vitro* cellular viability and proliferation of the DCH-*x* hydrogels were assessed according to ISO 10993-5 standard test method. Cell viability was assessed using [3-(4,5-dimethylthiazol2-yl)-1,5-diphenyltetrazulium bromide] (MTT, Sigma, USA) mitochondrial reaction. This test is based on the reduction of a tetrazolium-based compound, to a purplish formazan product by viable cells. In brief, the hydrogel samples were immersed in ethanol 70% for 30 min to be disinfected and subsequently washed in phosphate buffer saline (PBS) under sterile conditions. The samples were then stored at biological cabinet under UV light exposure overnight. The samples were placed into 24-well plates and NIH/3 T3 fibroblast cells were seeded at a density of 5×10^4 cells per well. The culture medium containing Dulbecco's modified eagle medium DMEM medium supplemented with 10% fetal calf serum (FCS) (Sigma, USA) was added and incubated at 37 °C and 5% CO_2 for 3 and 7 days. After incubation time, the samples washed three times with PBS, and MTT solution (5 mg/ml in PBS) was added to the samples. After 2 h incubation at 37 °C, the MTT solution was replaced by 0.5 ml of dimethylsulphoxide (DMSO) as the extracting solution. The absorbance of the supernatant was read by a microplate reader at 540 nm.

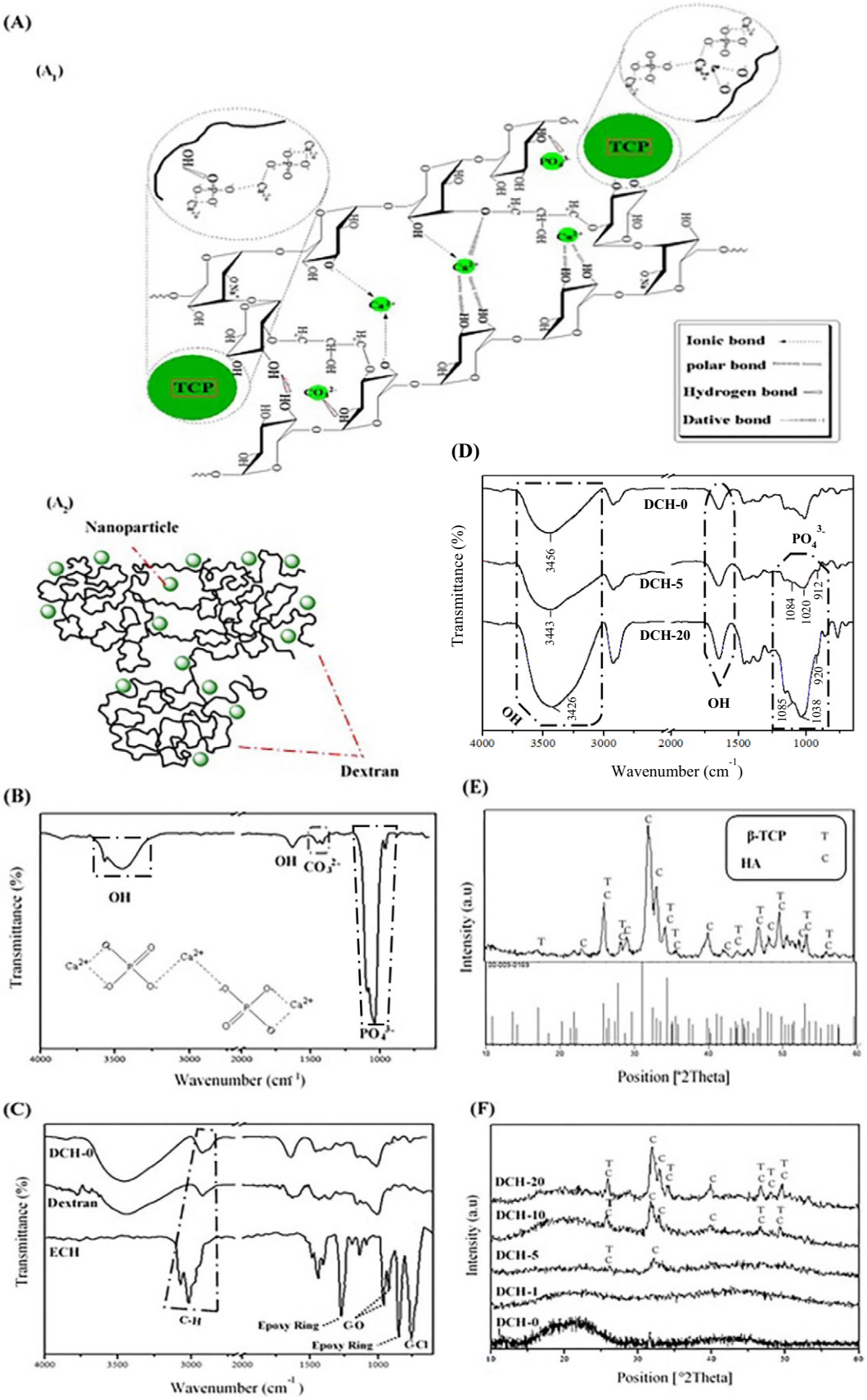

Fig. 2. (A) The probable interaction between dextran chains and β-TCP ions and β-TCP particles as fillers (A_1), and general view of the β-TCP particles as active fillers in dextran matrix (A_2). (B) FTIR spectrum of β-TCP, (C) FTIR spectra of ECH, pristine dextran, and DCH-0 and (D) FTIR spectra of DCH-0, DCH-5, DCH-20 and β-TCP. (E) XRD pattern of β-TCP and (F) XRD patterns of DCH-0, DCH-1, DCH-5, DCH-10 and DCH-20.

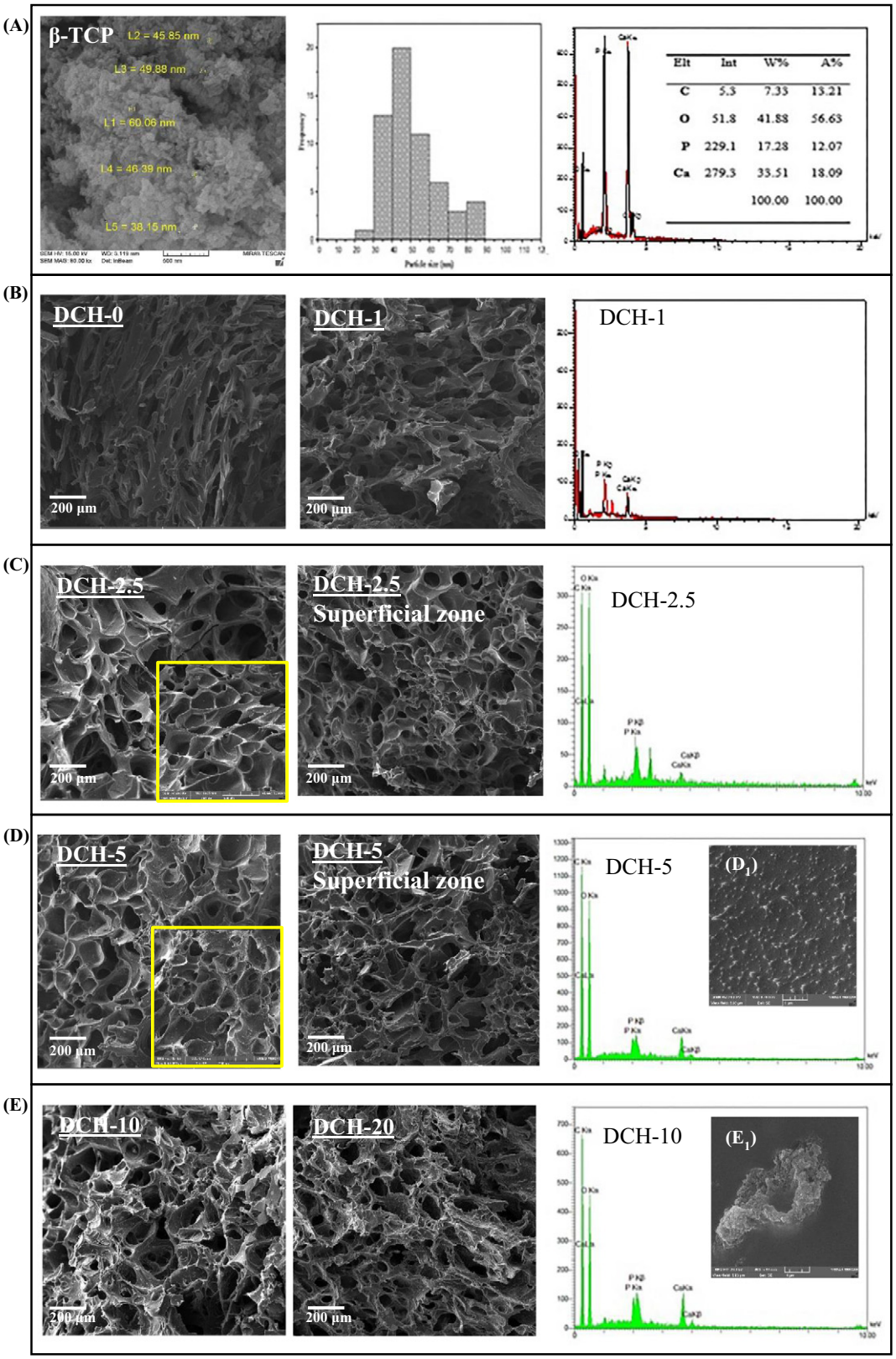
(A)
β-TCP
L2 = 45.85 nm
L3 = 49.88 nm
L1 = 60.06 nm
L4 = 46.39 nm
L5 = 38.15 nm
Elt Int W% A%
C 5.3 7.33 13.21
O 51.8 41.88 56.63
P 229.1 17.28 12.07
Ca 279.3 33.51 18.09
100.00 100.00
(B)
DCH-0
200 µm
DCH-1
200 µm
DCH-1
(C)
DCH-2.5
200 µm
DCH-2.5
Superficial zone
200 µm
DCH-2.5
(D)
DCH-5
200 µm
DCH-5
Superficial zone
200 µm
DCH-5
(D1)
(E)
DCH-10
200 µm
DCH-20
200 µm
DCH-10
(E1)

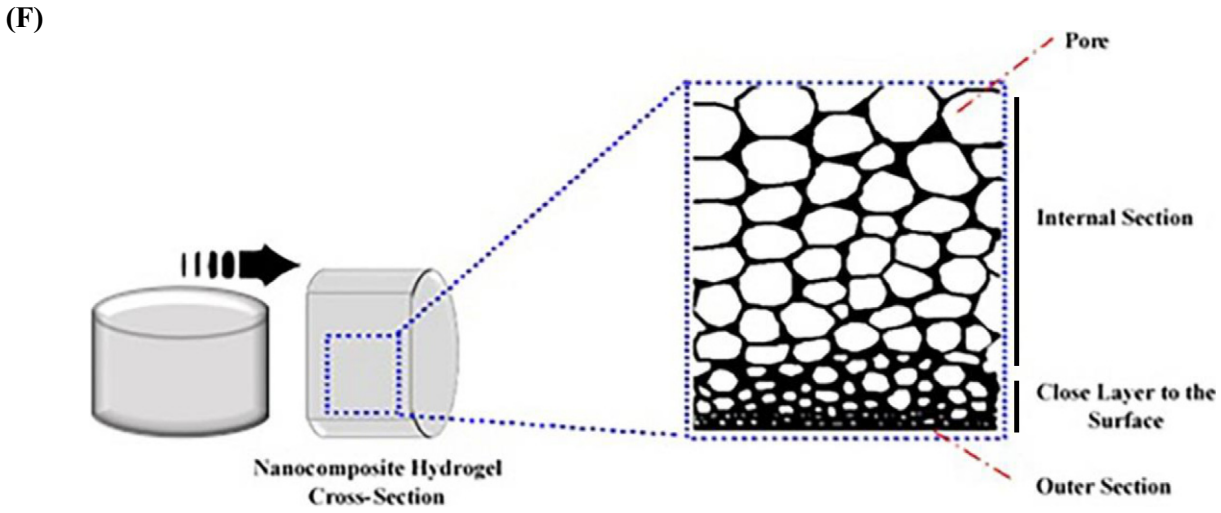

Fig. 3. (A) FESEM images of β-TCP particles, the histogram of β-TCP particles size distribution and EDX spectra indicating β-TCP particles elements and results of EDX analysis indicating β-TCP particles elements (panel A, inset). (B–D) SEM micrographs from the cross-section of DCH-*x* samples the different parts and EDX spectra of Ca, P, O and C elements, and SEM micrographs from the cross-section of DCH-*x* samples at higher magnification showing the nanoparticles distribution inside dextran matrix (panels D_1 and E_1, inside). (F) Schematic illustration of the two-layer morphology formed during the freeze-drying of DCH-*x* sample.

3. Results and discussion

3.1. Structural characterization of DCH-x samples

The formation of dextran hydrogel was simply investigated using the tube inversion test, as shown in Fig. 1(C). The test provides visual evidence that the initial dextran solution formed to the soft solid (gel) state after the crosslinking reaction.

The molecular structure of dextran/β-TCP nanocomposite hydrogels (DCH-*x*) has been shown in Fig. 2(A). As can be seen, the resultant hybrid network is formed through crosslinking of dextran chains with ECH and interactions among dextran chains and β-TCP nanoparticles. Study of these interactions is essential to interpret the swelling behavior of DCH and formation mechanisms of biomineralization processes in SBF.

The mechanism of dextran crosslinking under alkaline conditions has been previously described by Salimi-Kenari et al., in details [26,27]. The incorporation of β-TCP nanoparticles into the dextran matrix leads to inter and intramolecular interactions between the ceramic nanostructures and dextran chains during the crosslinking reaction. The schematic of probable interactions was shown in Fig. 2(A_1). Dextran possesses three OH functional groups per glucose residues in its chain structure, while β-TCP nanoparticles have calcium (Ca^{2+}) and phosphate (PO_4^{3-}) ions in their molecular structure. The presence of carbonate ion (CO_3^{2-}) in β-TCP crystalline structure was confirmed according to FTIR, EDX and XRD results (Fig. 2(b–f)). It is worthy of note that as β-TCP powder in micronized form is rapidly resorbable *in vivo*, it needs to be pretreated at high temperature through sintering to eliminate traces of impurities and increase resorbability time after implantation. However, traces of carbonate ions may not affect the final microstructure, physicomechanical, and bioactivity of DCH scaffolds. The possible interactions among dextran chains and β-TCP nanoparticles include ionic interactions between the ionized hydroxyl groups of dextran (O^-) in alkaline media with free adsorbed Ca^{2+} ions. Consequently, dextran hydroxyl groups possess a strong negative dipole that can chelate free Ca^{2+} in the alkaline solution and form a coordinated bond. Furthermore, PO_4^{3-} could bond with the dextran-associated calcium to form calcium-phosphate complexes. By further complexation with PO_4^{3-} could act as β-TCP filler nanoparticles. In addition, formation of ionic interactions between the O^- groups to Ca^{2+} present on the interface of β-TCP clusters and dextran matrix can be considered at the intermolecular scale. It should be noticed that hydroxyl groups have a hydrogen bonding affinity with P-OH groups in the interface of β-TCP clusters. In addition, the PO_4^{3-} ions could be absorbed onto OH groups of dextran by hydrogen bonding. [28–32].

FTIR analysis was performed to determine the functional groups involved in crosslinking reaction and other feasible interactions. FTIR spectra of β-TCP nanoparticles, pristine dextran, ECH, DCH-0, DCH-5, and DCH-20 are presented in Fig. 2(B–D). The FTIR spectra of β-TCP indicated peaks at 1040 and 1460 cm^{-1} corresponding to PO_4^{3-} and CO_3^{2-} vibration bonds, respectively [33]. The C—O bands of CO_3^{2-} group can be due to adsorption of atmospheric carbon dioxide.

As shown in Fig. 2(C), the appearance of absorption bands at 2924 cm^{-1} (C—H stretching), 1460 cm^{-1} (C—C stretching (ring)), 1014 cm^{-1} (C—O stretching) and 768 cm^{-1} (C—Cl stretching) for dextran hydrogel (DCH-0) and the remarkable decrease in the intensity of epoxy ring at 1276 and 857 cm^{-1} in comparison with ECH confirm the formation of DCH-0 *via* chemical crosslinking reaction [26,27,34].

Due to the complexity of the DCH-5 and DCH-20 spectra, we only focused on the adsorption bonds of Ca^{2+} and PO_4^{3-} with O—H peaks that are expected to be involved in the intermolecular interaction. It is worth to note that the observed peak at 3456 cm^{-1} for DCH-0, is assigned to hydrogen bonds of dextran chains (O—H stretching vibration); which shifts to lower wavelength for DCH-5 (3443 cm^{-1}) and DCH-20 (3426 cm^{-1}). The peaks displacement can be attributed to introduction of ionic interactions to the dextran chains, which inhibit intramolecular hydrogen [35]. By comparison of DCH-0 and DCH-5 spectra at 1645 cm^{-1}, it was found that addition of 5 *wt%* β-TCP shifts the adsorption peak to a higher wavenumber (1651 cm^{-1}). Furthermore, the peak representing PO_4^{3-} tetrahedral structure that usually appears in the composite formulations was shifted from 1040 cm^{-1} to 1020 cm^{-1}

Table 1
Pore size range and average of freeze-dried DCH-*x* scaffolds determined based on SEM image analysis.

Samples	Pore size range (μm)	Average pore size (μm)
DCH-0	74–135	97
DCH-1	50–98	71
DCH-2.5	118–190	144
DCH-2.5 (superficial zone)	51–155	103
DCH-5	120–200	150
DCH-5 (superficial zone)	30–110	67
DCH-10	65–135	105
DCH-20	50–132	89

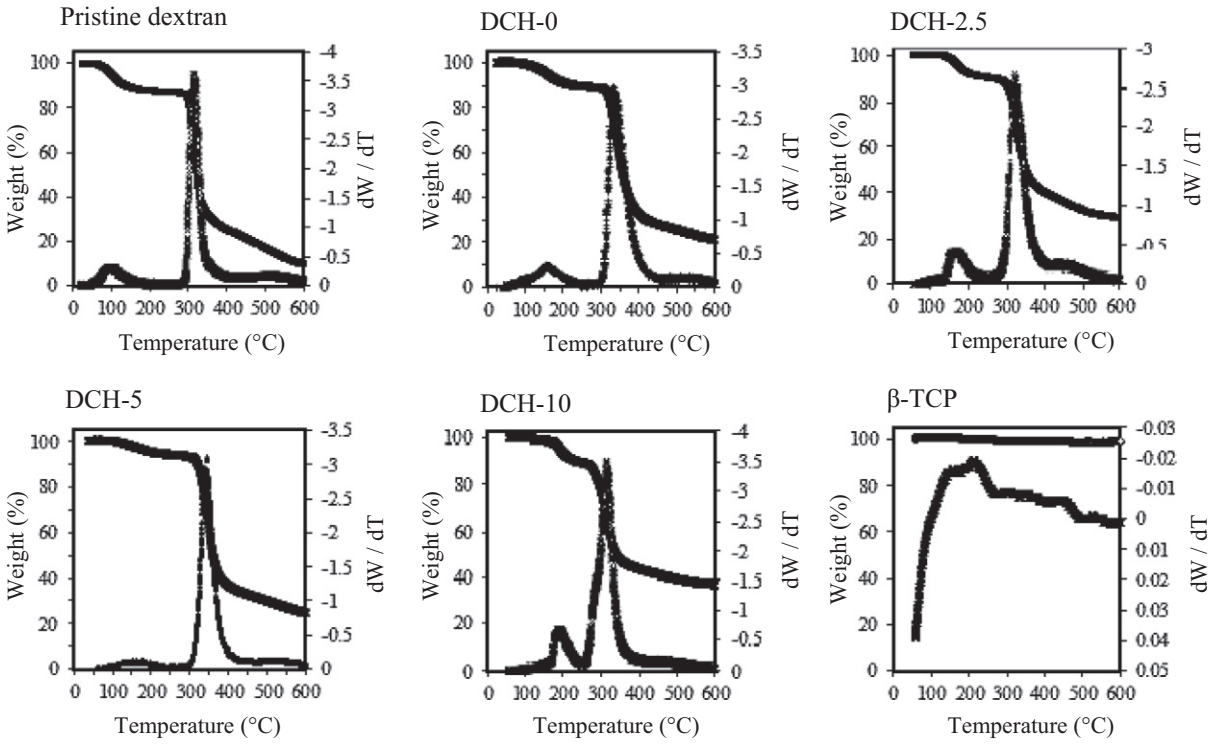

Fig. 4. Thermogravimetric analysis and derivative thermograms of pristine dextran, DCH-0, DCH-2.5, DCH-5, DCH-10 and β-TCP.

and 1038 cm^{-1} for DCH-5 and DCH-20, respectively. The observed peak displacement implies the interaction between PO_4^{3-} with O—H groups of dextran and water molecules, while some of the PO_4^{3-} prevented the O—H bending vibration. The observed peaks for DCH-20 are more intensive in the range of 950 cm^{-1} to 1050 cm^{-1}, which is attributed to higher amount of TCP ions interacting with dextran functional groups. In view of this, interfacial interactions of β-TCP clusters with dextran matrix can be conferred.

The XRD pattern of β-TCP in Fig. 2(E) confirms the crystalline phase of β-TCP nanoparticles. As seen, the β-TCP nanoparticle XRD peaks match well with the β-TCP standard JCPDS card No. 0169-009 at 17.08°, 26.24°, 28.47°, 34.45°, 35.92°, 47.10°, 48.47°, 49.80°, 50.89° and, 56.25° angels. The observed peaks in β-TCP pattern confirm the presence of calcium carbonate and hydroxyapatite phase, due to the presence of water molecules in β-TCP. The mean crystal size of calcium phosphate was calculated 33.6 nm by using the Scherrer's equation, by considering three sharp peaks at (2θ) angles of 26.24°, 32.5° and 33.25°.

The XRD pattern of DCH-0 shown in Fig. 2(F) exhibits a broad peak positioned between 15 and 30° (2θ), which confirms a general amorphous structure. The XRD pattern of DCH-1 showed no obvious crystalline structures because of the low content of β-TCP nanoparticles. This could be attributed to the polymeric-rich phase, which masks the crystalline β-TCP nanostructures. By increasing β-TCP content from 1 to 20 *wt%* sharp peaks appear at 25.79°, 31.85°, 32.96°, 33.99°, 39.95°, 46.67°, 48.1°, 49.53° and 55.93° angles, which show the increase in crystallite size. The crystal size of nanoparticles in DCH-5, DCH-10 and DCH-20 was calculated to be 15.2, 24.3 and 29.4 nm, respectively.

3.2. Morphological characterization of β-TCP nanoparticles and nanocomposite hydrogels

As revealed by FESEM characterization (Fig. 3(A)), β-TCP powder consists of nanoscale dense morphology with particle size ranging from 20 to 90 nm and average size of *ca.* 45.3 nm. Moreover, β-TCP nanostructures showed tendency to agglomerate and form cluster-like morphology. The average crystallite size calculated based on the Scherrer's equation using the XRD results was obtained equal to 33.6 nm, which was found to be well consistent with the average size of crystallite obtained *via* FESEM micrographs. The EDX spectra represented the peaks of Ca, P, C and O elements and their qualitative abundance (Inset Table in Fig. 3(A)) in β-TCP nanoparticles. In addition, the atomic ratio of Ca:P was estimated to be 1.49, which is close to the standard atomic ratio of 1.5 for β-TCP.

Fig. 3(B–D) shows the microstructure of the 3D porous DCH-*x* scaffolds fabricated using the freeze-drying technique. Obviously, the frozen adsorbed bulk water formed into ice crystals are removed by sublimation, leaving the pores behind. The polymer-rich phase, on the other hand, contained most of the polymer solution and formed cell walls around the pores. The cross-sections of the prepared DCH-*x* samples (Fig. 3(B–D)), show a 3D porous structure containing significant

Table 2
Results of thermal analysis obtained for pristine dextran and DCH-*x* samples.

Samples	Water removal temperature (°C)	Onset of thermal degradation temperature (°C)	Maximum rate decomposition temperature (°C)	Final of thermal decomposition temperature (°C)	Residual weight at 600 °C (*wt%*)
Pristine dextran	99	291	314	335	10%
DCH-0	166	230	334	377	20%
DCH-2.5	170	293	325	360	30%
DCH-5	175	314	343	364	28%
DCH-10	192	276	314	345	38%

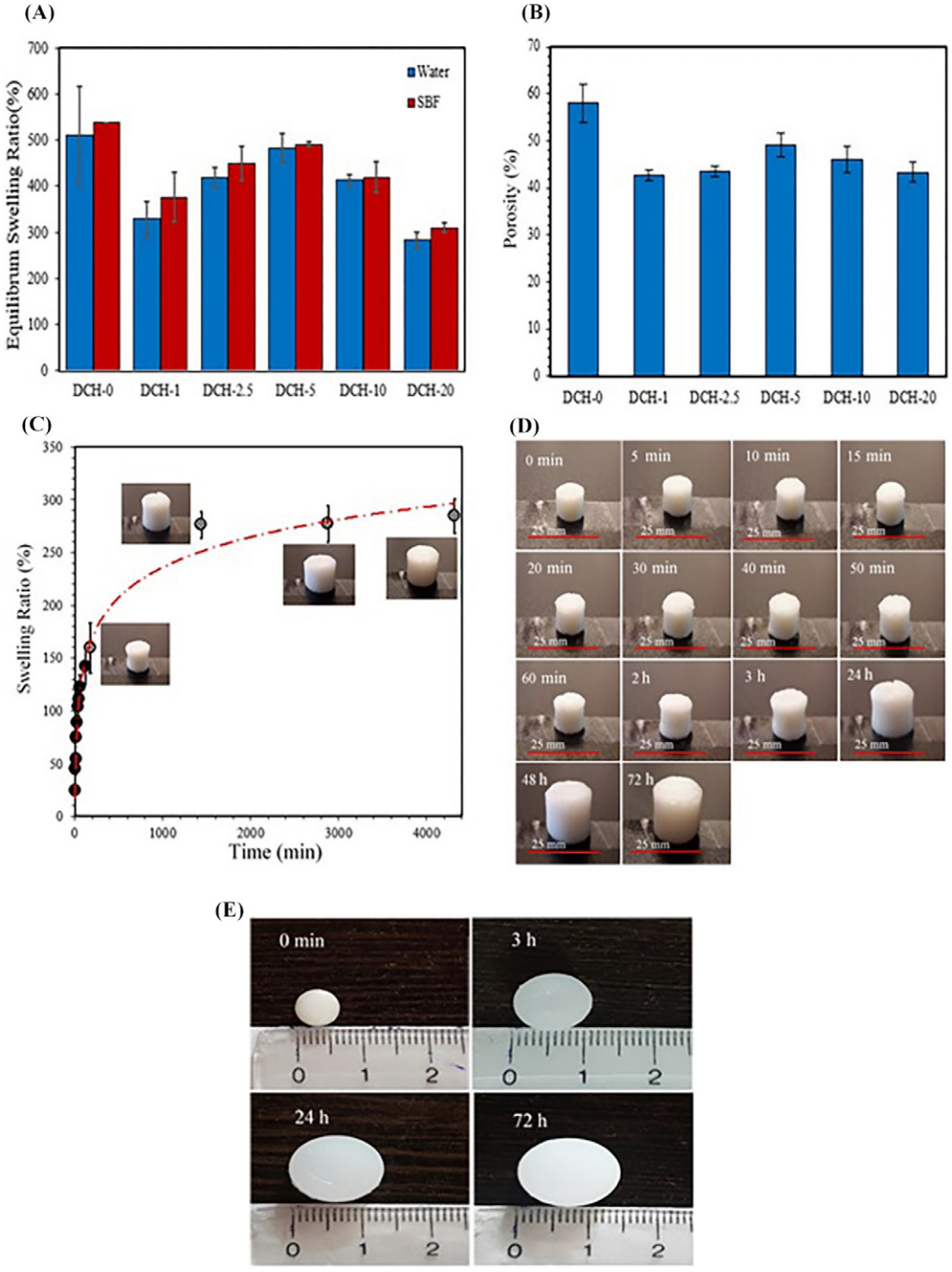

Fig. 5. (A) Equilibrium swelling ratio of DCH-*x* hydrogels in deionized water and simulated body fluid (SBF); (B) porosity of DCH-*x* hydrogels as a function of β-TCP content; (C) swelling ratio of DCH-20 hydrogel in deionized water as a function of time; The visual observation of water uptake behavior and dimensional stability of (D) DCH-20, and (E) DCH-5 hydrogels in deionized water at various time intervals.

differences in the pore morphologies for DCH-0 and other composite samples. It is worth to note that ideal scaffolds for bone tissue engineering should be able to support the dynamic microenvironment of tissue, which is constantly developing and remodeling its matrix to regenerate the new mineralized bone matrix. It has been shown that scaffolds with interconnected pores of over 300 μm can facilitate cells migration, vascularization, and tissue ingrowth. The SEM micrographs of DCH-2.5 and DCH-5 scaffolds in Fig. 3(C, D) show pores in the range of 200 μm. However, the interconnectedness of these pores could not be evaluated in the present study.

As can be seen, the pore morphologies of composite hydrogels containing different β-TCP content are more uniform with a spherical cellular structure and some regions of interconnectivities when magnified. The dextran hydrogel (Fig. 3(B)) consisted of non-uniform collapsed pores which further shrink after the lyophilization process. Microstructural alteration in DCH-*x* matrices was observed with increasing β-TCP nanoparticles content, and the highest porosity was obtained for the DCH-5 scaffold. As the freeze-drying conditions were identical for all samples, the various pore size and microstructure of DCH-*x* matrices originates from their different physicochemical properties. As

illustrated in Fig. 3(B, C) and Table 1, pore size average significantly increases from 71 μm for DCH-0 to 144 μm and 150 μm for composite scaffolds containing 2.5 and 5 *wt%* β-TCP, respectively. Such observation could be attributed to the higher water uptake capacity of nanocomposite hydrogels due to formation of less crosslinked networks, which results in larger mean pore size diameter. These results agree with Fan et al., reported studies on controlled porous structure of polyimide/carbon nanotube composite aerogels. They found that pores size is highly dependent on the crosslinking points formed during the gelation process [36]. Zhang et al. have also reported a similar observation for the hydroxypropyl cellulose composite hydrogels [37]. It can be further explained by considering the inter-chain crosslinking of polymer chains,

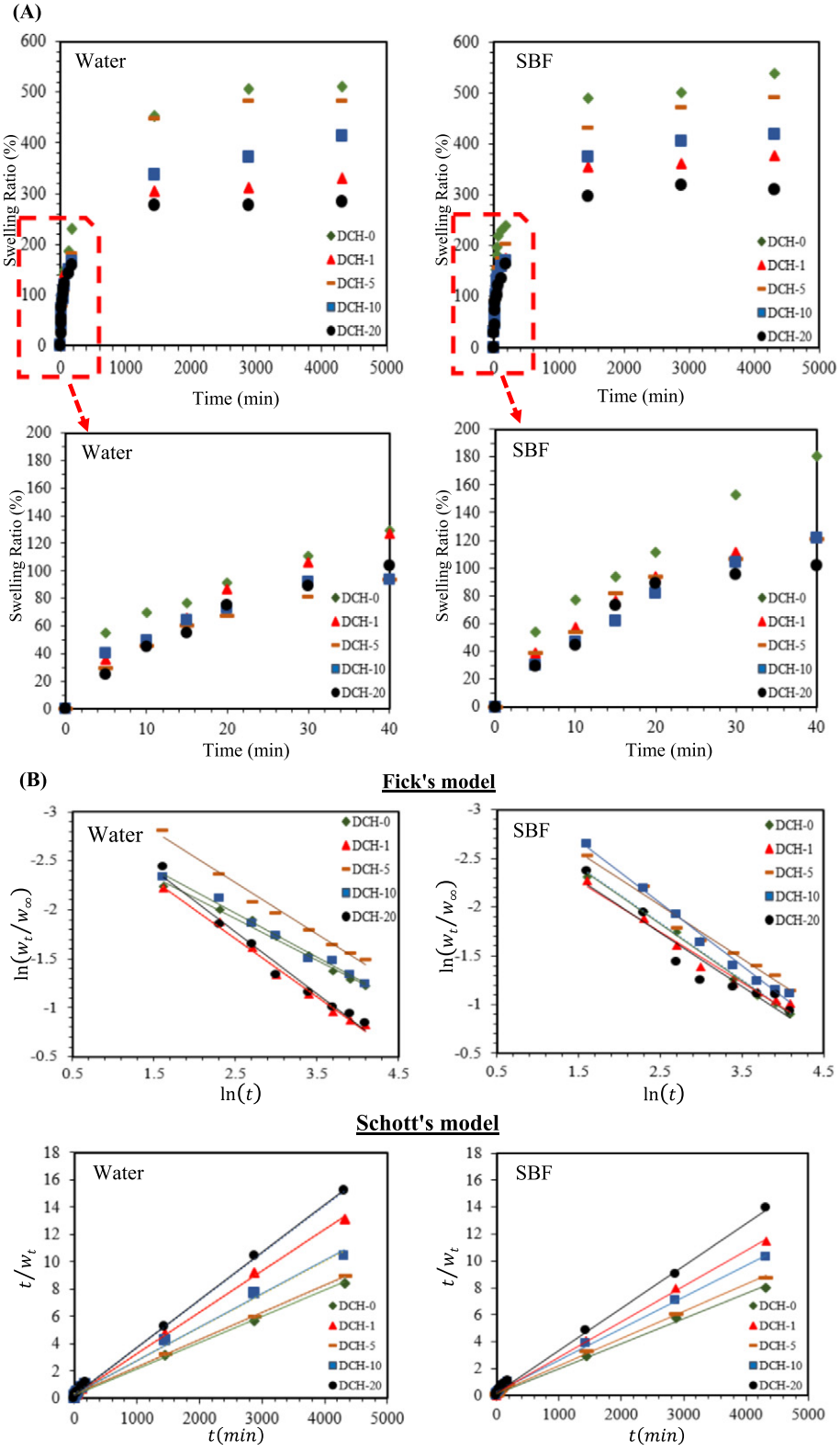

Fig. 6. (A) Experimental swelling ratio plotted *versus* time for DCH-*x* in deionized water and SBF solutions (up) at equilibrium state (down) initial stage of swelling at 40 min, (B) By using Fick's first-order (Eq. (4)) and Schott's second-order (Eq. (5)) swelling kinetics models the swelling data of DCH-*x* scaffolds are displayed and fitted.

which compete with the force of the ice crystal growth and the capillary force during ice sublimation. By further increasing content of β-TCP nanoparticles to 10 and 20 *wt*%, a decrease in mean pore size to 105 and 89 μm was found, respectively. A possible explanation is agglomeration of β-TCP nanoparticles which can be seen in Fig. 3(E_1). In other words, taking the pore space by β-TCP agglomerates results in reduced pore size diameter [38]. As displayed in Fig. 3(E), β-TCP nanostructures are evenly distributed on the wall of scaffold pores. Moreover, it can be seen that in comparison with apparently dense DCH-0 pore wall with a smooth surface, the pore wall of composite scaffolds appears thicker due to the embedded β-TCP agglomerates.

As presented in Fig. 3(F), a gradient pore size was observed for the DCH-*x* scaffolds. Scaffolds with gradient pore size have shown great potential for guided tissue regeneration [39]. It has been shown that gradient pore size scaffolds can accommodate two of more cell types, which offer multi-tissue (*e.g.*, osteochondral interface) regeneration [40]. An average pore size of 67 and 150 μm was observed for the regions in the vicinity of outer layer (superficial zone) and inner sections (bulk) of DCH-5, respectively (Fig. 3(C, D)). The gradient pore size in the bulk and surface originates from the difference in the cooling and sublimation rate induced by the freeze-drying process. As the cooling rate is faster in the superficial regions during the freezing process, ice crystals are limited to grow which diminishes pore size diameter. On the other hand, in the bulk region where ice crystals have longer time to grow form larger pore size [41,42]. It should be notified that EDX spectra of DCH-*x* scaffolds (Fig. 3(D)) confirm the incorporation of nanoparticles into the dextran matrix.

3.3. Thermal analysis

The thermal behavior of β-TCP, pristine dextran and composite hydrogels (DCH-0, DCH-2.5, DCH-5 and DCH-10) were investigated by thermogravimetric analysis (Fig. 4 and Table 2) to describe the interactions among dextran chains and β-TCP clusters. As shown in Fig. 4, a three-step thermal decomposition process is observed for all samples. The first step of weight loss at 25–200 °C is assigned to the removal of the bound water to the polymer network. The higher moisture loss temperature of 192 °C observed for DCH-10 compared to 99 °C for the pristine dextran is attributed to the chain mobility restraints induced by the crosslinking reaction. In the case of composite scaffolds, water loss temperature was found to shift to higher range by incorporating β-TCP nanoparticles, suggesting improved interactions between water molecules with phosphate groups of β-TCP.

The second step of weight loss where the main decomposition occurred attributes to the degradation of polysaccharide structure of dextran and crosslinking bonds. The lower onset temperature of decomposition for DCH-0 compared with pristine dextran can be ascribed to the various bond strength between crosslinked backbone and intramolecular covalent bonds in dextran chains [15]. The higher onset decomposition temperature for DCH-2.5 and DCH-5 is attributed to a homogeneous dispersion of β-TCP nanoparticles in the polymer matrix. However, relatively lower onset decomposition temperature in the case of DCH-10 might be because of formation of local hotspots due to the agglomeration of the nanoparticles. The higher maximum degradation rate of pristine dextran compared to DCH-0 is thanks to the role of ECH to chemically crosslink dextran chains. Among DCH formulations, the highest onset and maximum decomposition temperatures were obtained for DCH-5. The improved thermal stability of DCH-5 matrix relies on the homogeneous dispersion of β-TCP nanoparticles acted as a protective barrier for the organic phase against thermal degradation.

The higher residual weight of DCH hydrogels after decomposition again confirms the physical interaction and consequently stability of β-TCP nanoparticles in dextran matrix.

Table 3
Swelling parameters obtained from Fick's model for DCH-*x* scaffolds.

Hydrogel	Water			SBF		
	k (g/g·min)	n	R^2	k (g/g·min)	n	R^2
DCH-0	0.051	0.423	0.989	0.037	0.582	0.989
DCH-1	0.041	0.591	0.990	0.047	0.516	0.98
DCH-5	0.027	0.522	0.988	0.034	0.544	0.978
DCH-10	0.046	0.445	0.989	0.026	0.641	0.988
DCH-20	0.034	0.631	0.981	0.044	0.552	0.92

The regression equation for each sample is Y = A + BX (Y = **ln** ($W_t/W\infty$), A = **ln** k, B = n, x = **ln t**).

Table 4
The swelling parameters obtained from Schott's model for DCH-*x* scaffolds.

Hydrogel	Water				SBF			
	k_{is} (g/g·min)	W_∞ (g/g) (%)	W_{eq} (g/g) (%)	R^2	k_{is} (g/g·min)	W_∞ (g/g) (%)	W_{eq} (g/g) (%)	R^2
DCH-0	4.415	526	511	0.999	6.253	526	538	0.996
DCH-1	4.399	333	329	0.998	4.275	384	376	0.998
DCH-5	3.174	500	483	0.996	4.034	500	491	0.997
DCH-10	3.109	416	413	0.993	3.687	434	419	0.997
DCH-20	4.003	285	284	0.999	3.986	322	309	0.998

The regression equation for each sample is Y = A + BX (Y = t/Wt, A = $1/k_{is}$, B = $1/W_\infty$, x = t).

3.4. Water uptake studies

The equilibrium swelling ratio of DCH-*x* hydrogels in deionized water and simulated body fluid (SBF) has been shown in Fig. 5(A). It was found that DCH-*x* scaffolds have a relatively higher uptake capacity in SBF than deionized water. This effect is due to the presence of free counter ions (*e.g.* Na^+, K^+, Ca^{2+}, Mg^{2+}, Cl^-, HCO_3^-, HPO_4^{2-} and SO_4^{2-}) in SBF medium, which increase osmotic pressure and induce water penetration into the gel matrix [43–45]. The chemical structure of the SBF containing Na^+, K^+, Ca^{2+}, Mg^{2+}, Cl^-, HCO^{3-}, HPO_4^{2-} and SO_4^{2-} ions can be responsible for the observed differences. These ions interact with the β-TCP nanoparticles and chains of the dextran, so modifying the nanoparticles and polymer interface with the solution [45]. For composite samples, Ca^{2+} ions would be released from β-TCP, into SBF *via* an exchange with the H_3O^+ ions in the solution to form OH groups on its surface [46] These OH groups would then combine with positively charged ions in SBF to form complex. The disconnection of the intermolecular bond of dextran chains by complex transferred into SBF leads to more flexible chains, which it can uptake more water.

Generally, the driving force for the water uptake of a hydrogel includes at least three components including the internal elastic force of polymer chains in network, polymer-water mixing, and osmotic pressure. In this view, the interplay of three balancing forces determines the equilibrium swelling ratio. Mixing pressure is due to solvation of network, while the elastic pressure is stretching polymer chains under the influence of solvation. The ionic pressure originates from mobility of ions between the hydrogel matrix and medium. The internal elastic force of polymer chains in the hydrogel network is strongly dependent on the crosslinking density, and interactions between polymeric chain segments and solvent molecules. While loosely crosslinked hydrogels fail to retain water, a highly crosslinked polymer network does not swell. Introduction of structural heterogeneity, such as hydrophilic tunnel or porosity, accelerates water diffusion in hydrogels, which improves the polymer water mixing and solvent diffusion rate. Solvent diffusion rate and chain relaxation rate are also enhanced by introduction of ionic groups to the polymer backbone. Furthermore, a capillary force can be harnessed if microscale, interconnected pores can be generated in the hydrogel to act as an additional driving force to accelerate solvent diffusion.

The effect of β-TCP content on water uptake showed a similar trend both in deionized water and SBF (Fig. 5(A)). The highest ESR observed

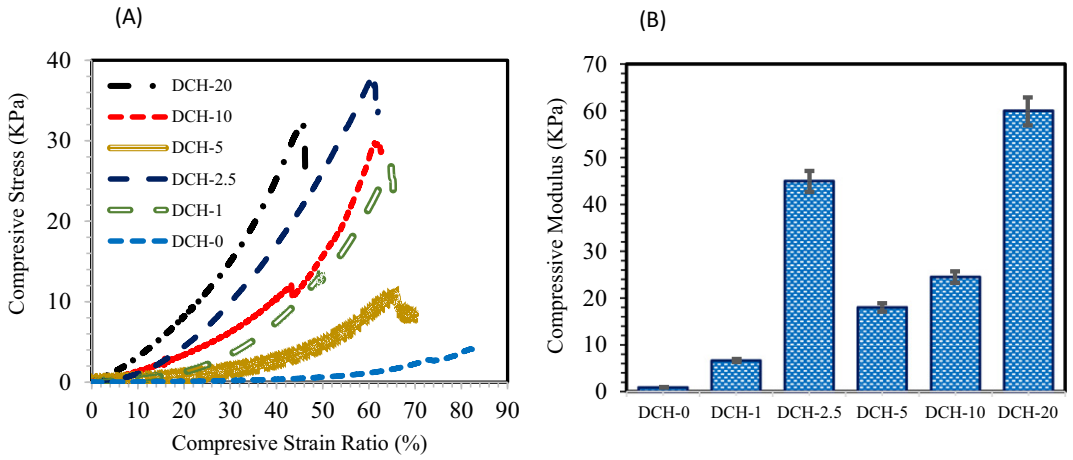

Fig. 7. (A) Stress–strain curves for swollen DCH-*x* scaffolds, (B) Compressive Modulus for swollen DCH-*x* scaffolds with various compositions.

for DCH-0 (ESR_{water} = 511% and ESR_{SBF} = 538%) in the absence of β-TCP can be attributed to the physical interaction of ceramic nanoparticles with polymeric phase, which hinders dextran chains stretching in the course of swelling. In other words, decreased ESR in the case of DCH-1 (ESR_{water} = 329% and ESR_{SBF} = 376%) in comparison with DCH-0 hydrogel is ascribed to the role of β-TCP as a physical crosslinker between dextran chains, which reduce porosity to 42.7% from 58% for DCH-0 (Fig. 5(A)). ESR of DCH scaffolds increased with increasing the content of β-TCP from 1 to 5, which is well consistent with the porosity trend for the corresponding samples. This effect suggests that the role of well-dispersed β-TCP in reduced crosslinking density and elastic contribution of polymer network is more pronounced. However, further increment of β-TCP content from 5 to 10 and 20 *wt%* was found to decrease water uptake. Such observation can be explained in terms of reduced porosity and retarded swelling in the presence of β-TCP agglomerates [47]. This result demonstrated that samples swelling ability was strongly affected by physical crosslinking and thereby the decrease in porosity. This finding was parallel to the results reported [47] for other composite hydrogels. On the other hand, the elastic contribution varied mainly with change in effective network density and mix contribution played an influential role in regulating the water uptake of samples.

Swelling of DCH scaffolds immersed in deionized water and SBF was monitored as a function of time. As seen in Fig. 5(C), DCH-20 swells rapidly in the first 24 h, and then swelling rate becomes slower until ESR is reached. The visual observation of water uptake behavior and dimensional stability of DCH-5 and DCH-20 over 72 h are depicted in Fig. 5 (D, E).

Swelling kinetics of DCH scaffolds in deionized water and SBF have been shown in Fig. 6(A). Swelling rate of DCH-0 was found to exceed scaffolds comprising β-TCP. While DCH-1 showed the highest swelling rate in deionized water among composite scaffolds, no significant difference was observed in SBF. To get an insight into the water uptake behavior of scaffolds, their swelling kinetics was analyzed with Fickian and Schott kinetics models.

According to the Fick's model, the swelling kinetics in the initial stage of swelling ($W_t/W_\infty \leq 0.6$) could be determined with the following equation:

$$W_t/W_\infty = kt^n \tag{4}$$

where W_t and W_∞ represent water swelling capacity of the hydrogel at time t and equilibrium, respectively, k is the initial swelling rate constant, and n is the diffusion index calculated from the slopes of $\ln(W_t/W_\infty)$ as a function of $\ln(t)$ (Fig. 6(B)). Generally, at $n \leq 0.5$, Fickian diffusion plays the decisive role (*i.e.* rate of diffusion (R_{dif}) ≪ polymer chains relaxation (R_{rel})), $0.5 < n < 1.0$ corresponds to non-Fickian diffusion in which the rate of diffusion and the rate of polymer chains relaxation are comparable ($R_{dif} \sim R_{rel}$), and $n = 1$ the relaxation of polymer chains plays the leading role ($R_{dif} \gg R_{rel}$) [48,49].

The swelling kinetic parameters based on Fick's model are summarized in Table 3. The swelling kinetics showed relatively low correlation coefficient (R^2) to Fickian model.

In the Fick's model, the diffusion coefficient of penetrating agent and film thickness are assumed to remain constant during swelling. As the scaffolds thickness does not remain constant, their swelling pattern was interpreted by Schott's swelling kinetic model. This model considers a second-order correlation for the swelling kinetics. Schott's swelling model is defined based on the following equation:

$$(t/W_t) = (1/k_{is}) + (1/W_\infty)t \tag{5}$$

where W_t is the swelling at time t, W_∞ is the theoretical equilibrium swelling, and k_{is} is the initial swelling rate constant.

The swelling kinetic parameters based on Schott's model and t/W_t *versus* t plots in Fig. 6(B) are summarized in Table 4. Accordingly, higher correlation coefficients were obtained both in deionized water and SBF solutions (>0.99). The theoretical equilibrium swelling ratio in Schott model values (W_∞) was approximately equal to ESR (W_{eq}). The initial swelling rate in Schott's model is related to the rate of polymer chains relaxation, which is affected by the following factors: the hydrophobicity/hydrophilicity, the degree of crosslinking, the rigidity/flexibility, the amorphous regions/crystalline domains and the thickness of hydrogel [48,49]. The trend of the initial swelling rate constant (k_{is}) was obtained as follows, DCH-0 > DCH-1 > DCH-20 > DCH-5 > DCH-10, which can be attributed to the number of free hydroxyl groups on dextran chains in the DCH-*x* matrices to interact with aqueous media [50]. The highest k_{is} obtained for DCH-0 confirms this postulation. k_{is} was found to decrease with increasing β-TCP content, due to their interaction with dextran hydroxyl groups. However, the higher k_{is} in the case of DCH-20 can be interpreted in terms of the nanoparticles agglomeration to decrease their interface with polymer matrix and their water retention feature. Therefore, lower k_{is} value for DCH-5 could be related to the better dispersion of the β-TCP nanoparticles in dextran matrix observed in Fig. 4(B), which probably affects both on decrease free OH groups of dextran and interaction between polymer chains. According to Zhao reports, increase the crosslinking density the more interaction between polymer chains should reduce the k_{is} value. However, the hydrophilicity was a more important effect on the initial swelling rate for hydrogels than the crosslinking density [50]. It is worth to note that relatively higher k_{is} in SBF than water is ascribed to higher osmotic pressure in SBF.

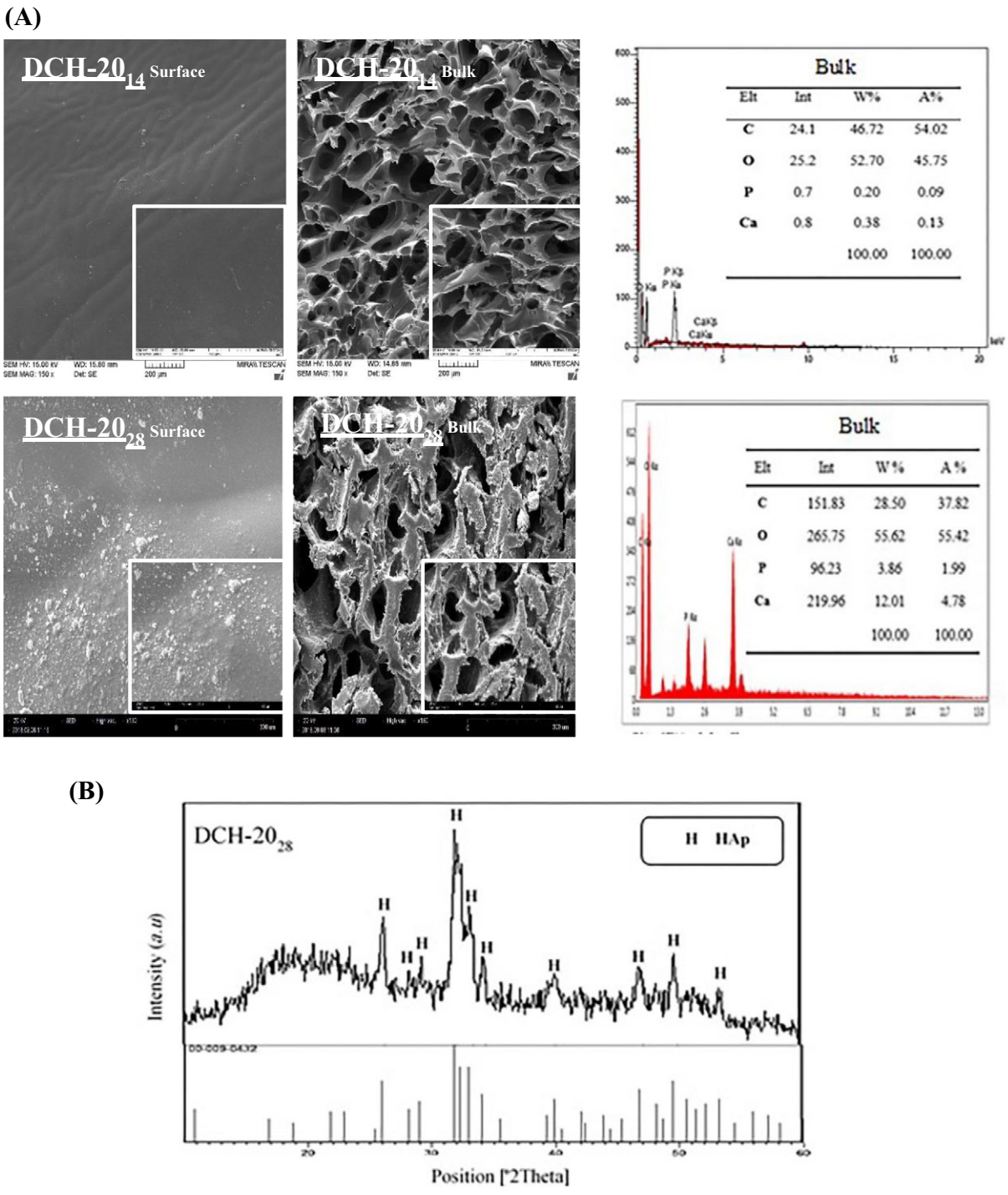

Fig. 8. (A) SEM micrographs of surface and bulk of DCH-20 scaffold immersed in SBF after 14 (DCH-20_{14}) and 28 (DCH-20_{28}) days; The EDX spectra of Ca, P, O and C elements in bulk of scaffolds are displayed in the right panel. XRD pattern of DCH-20_{28}.

3.5. Mechanical properties

In addition to swelling behavior and morphological characteristics, the mechanical properties of scaffolds have been identified as an important functionality for tissue engineering applications [51]. Hence, the influence of TCP content on the mechanical properties of DCH scaffolds was characterized. The stress-strain curves of swollen DCH scaffolds and their compressive modulus are displayed in Fig. 7(A, B). As can be seen, the incorporation of TCP significantly enhanced the compressive modulus of the dextran matrix. Such an increase in compressive stress can be attributed to the interfacial interactions between the inorganic and organic components. Swollen DCH-2.5 scaffold was found to have the highest compressive modulus among scaffolds with TCP content in the range of 1–10 *wt%*, while DCH-20 showed higher compressive modulus.

Although the reinforcement of DCH scaffolds with TCP particles (20 *wt%*) has contributed to improving in the compressive modulus up to 60 KPa, the prepared composite scaffolds have obviously shown lower compressive modulus compared to the desired value for the natural bone [52,53]. Then, the prepared scaffolds can be qualified for non-

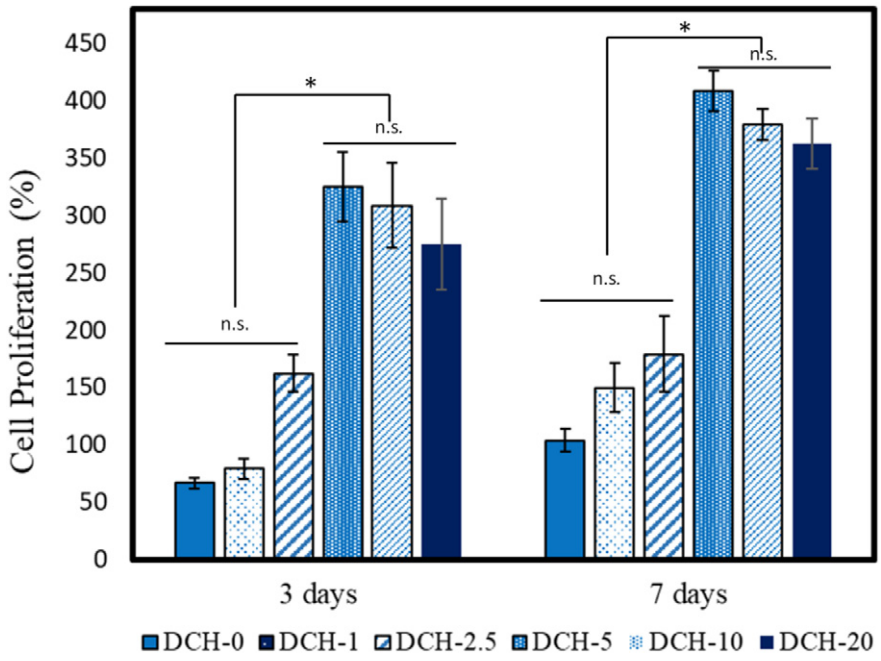

Fig. 9. Cellular proliferation on the dextran composite hydrogels (DCH) comprising 0, 1, 2.5, 5, 10 and 20 *wt%* of β-tricalcium phosphate (β-TCP) nanoparticles (DCH-0, DCH-1, DCH-2.5, DCH-5, DCH-10 and DCH-20) compared to the tissue culture dish as the control group at 3 and 7 days assessed by MTT assay.

load-bearing applications such as some treatments of oral and maxillofacial defects [54]. A further improvement of the mechanical properties is proposed by better processing, mainly a better dispersion of the TCP particles in the DCH matrix.

3.6. Biomineralization and cellular activity studies

DCH scaffolds were characterized for their biomineralization capacity *in vitro*. To this end, scaffolds were incubated in SBF to assess the apatite nucleation and growth. Fig. 6(A) shows the SEM micrographs of surface and bulk of DCH-20 scaffold immersed in SBF after 14 (DCH-20_{14}) and 28 (DCH-20_{28}) days. As illustrated, mineralization has occurred after 28 days on both surface and bulk of the scaffold. Lei et al. reported formation of HAp crystals on the surface of the polycaprolactone-β/TCP scaffolds after 17 days of immersion in SBF solution [46]. The release and dissolution of β-TCP nanoparticles in DCH-20_{14} can justify the formation of smooth surfaces after 14 days, which leads to local change in ions essential for HAp crystals precipitation. Hence, new HAp crystals formation was observed in DCH-20_{28}. According to the mechanics of formation of apatite, Ca^{2+} ions in SBF provided by the dissolving of composite surfaces; and then OH^- was accumulated gradually due to Ca^{2+} and H^+ exchange, which results in the increase of pH. When Ca^{2+} and PO_4^{3-} concentration on the sample reaches the threshold for nucleation, the crystallization occurs. In should be noticed that dissolution and precipitation of calcium phosphate crystals and formation of apatite layer took place concurrently.

The EDX spectra of DCH-20_{14} and DCH-20_{28} scaffolds in Fig. 8(A) indicate the formation of HAp. The Ca:P ratio for DCH-20_{14} and DCH-20_{28} was obtained as 1.45 and 2.4, respectively. Fig. 6(B) shows the XRD pattern of DCH-20_{28}, which is consistent with the patterns of the HAp standard JCPDS card No. 0432-009 at 26.16°, 28.26°, 29.21°, 32°, 33.33°, 34.34°, 39.9°, 46.97°, 49.81° and 53.39°. The mean crystal size of HAp was calculated 23.9 nm, by considering three sharp peaks at (2θ) angles of 26.16°, 32° and 33.33°. The obtained results indicate that bioactive bone-like apatite can form on scaffolds immersed in SBF.

The cell proliferation activity was studied by MTT assay. The viability of cells cultured on the DCH and hybrid hydrogel scaffolds containing 1, 2.5, 5, 10 and 20 *wt%* β-TCP over 7 days has been compared in Fig. 9. The statistical analysis showed that the number of cells significantly increased from 3th day to 7th day in all groups ($p < 0.05$). It was found that the hybrid hydrogel scaffolds containing 5, 10 and 20 *wt%* β-TCP significantly increase cell proliferation compared to the DCH-0 hydrogel and DCH-1 and DCH-2.5 composite scaffolds after 3 and 7 days. It should be noticed that no significant difference was observed between DCH-1 and DCH-2.5, as well as among DCH-5, 10, and 20 scaffolds after 7 days ($p < 0.05$). Such an observation could be justified by that the incorporation of the appropriate amount of β-TCP nanoparticles into the dextran matrix, enhancing cellular activity like cell adhesion, spreading and function. In accordance with our results, it has been described that powder incorporation of bioceramics such as β-TCP enhances the surface activity to interact with body fluids and produces active sites for cellular anchorage and mineral precipitation [55–57].

4. Conclusion

A series of dextran hydrogels and the dextran composite hydrogels (DCH) comprising different content of β-tricalcium phosphate (β-TCP) nanoparticles were prepared using the chemical crosslinking reaction. The incorporation and physical bond of β-TCP nanostructures into the dextran matrix were confirmed through FTIR spectroscopy and thermogravimetric analysis. Scanning electron microscopy of nanocomposites microstructure revealed that inclusion of β-TCP nanoparticles content determines the pore size and structure of the composite hydrogels, which is originated from the organic/inorganic interfacial interactions during the gelation process. Composite hydrogels comprising 5 *wt%* β-TCP nanoparticles (DCH-5) exhibited the highest porosity among DCH matrices. The swelling behavior of DCHs was found to be consistent with the surface porosity and pores size. Further, the higher water-absorbing capacity of DCHs in simulated body fluid solution in comparison to that of deionized water solution ascribed to higher osmotic pressure and capability of DCH matrix to absorb ions. The experimental data agreed with the proposed swelling kinetic model, and the diffusion of water into the hydrogels was non-Fickian during the initial stage of water uptake process. The Schott second-order kinetic model was found to describe the DCH water uptake behavior. Bioactivity studies showed that DCHs are capable of biomineralization in the simulated physiological condition. Cell culture studies confirmed that hydrogels could maintain cell activity and support cell growth *in vitro*.

CRediT authorship contribution statement

Rahil Ghaffari: Investigation, Data curation, Formal analysis, Writing - original draft. **Hamed Salimi-Kenari:** Supervision, Validation, Conceptualization, Writing - review & editing. **Farahnaz Fahimipour:** Investigation, Methodology. **Sayed Mahmood Rabiee:** Funding acquisition, Resources. **Hassan Adeli:** Data curation, Formal analysis. **Erfan Dashtimoghadam:** Conceptualization, Writing - review & editing.

References

[1] A. Khojasteh, F. Fahimipour, M. Jafarian, D. Sharifi, S. Jahangir, F. Khayyatan, M. Baghaban Eslaminejad, Bone engineering in dog mandible: coculturing mesenchymal stem cells with endothelial progenitor cells in a composite scaffold containing vascular endothelial growth factor, J. Biomed. Mater. Res. B Appl. Biomater. 105 (7) (2017) 1767–1777.

[2] M. Razavi, M. Fathi, O. Savabi, S.M. Razavi, F. Heidari, M. Manshaei, D. Vashaee, L. Tayebi, In vivo study of nanostructured diopside ($CaMgSi_2O_6$) coating on magnesium alloy as biodegradable orthopedic implants, Appl. Surf. Sci. 313 (2014) 60–66.

[3] E. Dashtimoghadam, G. Bahlakeh, H. Salimi-Kenari, M.M. Hasani-Sadrabadi, H. Mirzadeh, B. Nyström, Rheological study and molecular dynamics simulation of biopolymer blend thermogels of tunable strength, Biomacromolecules 17 (11) (2016) 3474–3484.

[4] S. Van Vlierberghe, P. Dubruel, E. Schacht, Biopolymer-based hydrogels as scaffolds for tissue engineering applications: a review, Biomacromolecules 12 (5) (2011) 1387–1408.

[5] C.-W. Chang, Y.-R. Wu, K.-C. Chang, C.-L. Ko, D.-J. Lin, W.-C. Chen, In vitro characterization of porous calcium phosphate scaffolds capped with crosslinked hydrogels to avoid inherent brittleness, Ceram. Int. 44 (2) (2018) 1575–1582.

[6] N. Pa'e, M.H. Salehudin, N.D. Hassan, A.M. Marsin, I.I. Muhamad, Thermal behavior of bacterial cellulose based hydrogels with other composites and related instrumental analysis, Cellulose-Based Superabsorbent Hydrogels 1 (2018) 763–787.

[7] F. Fahimipour, E. Dashtimoghadam, M.M. Hasani-Sadrabadi, J. Vargas, D. Vashaee, D.C. Lobner, T.S.J. Kashi, B. Ghasemzadeh, L. Tayebi, Enhancing cell seeding and osteogenesis of MSCs on 3D printed scaffolds through injectable BMP2 immobilized ECM-mimetic gel, Dent. Mater. 35 (7) (2019) 990–1006.

[8] F. Afriani, K. Dahlan, S. Nikmatin, O. Zuas, Alginate affecting the characteristics of porous beta-TCP/alginate composite scaffolds, Journal of Optoelectronics and Biomedical Materials 7 (3) (2015) 67–76.

[9] J. Puértolas, J. Vadillo, S. Sánchez-Salcedo, A. Nieto, E. Gómez-Barrena, M. Vallet-Regí, Compression behaviour of biphasic calcium phosphate and biphasic calcium phosphate–agarose scaffolds for bone regeneration, Acta Biomater. 7 (2) (2011) 841–847.

[10] S. Saravanan, R.S. Leena, N. Selvamurugan, Chitosan based biocomposite scaffolds for bone tissue engineering, Int. J. Biol. Macromol. 93 (2016) 1354–1365.

[11] Y. Yin, F. Ye, J. Cui, F. Zhang, X. Li, K. Yao, Preparation and characterization of macroporous chitosan–gelatin/β-tricalcium phosphate composite scaffolds for bone tissue engineering, J. Biomed. Mater. Res. A 67 (3) (2003) 844–855.

[12] Y. Liu, M.B. Chan-Park, Hydrogel based on interpenetrating polymer networks of dextran and gelatin for vascular tissue engineering, Biomaterials 30 (2) (2009) 196–207.

[13] X. Wang, Z. Li, T. Shi, P. Zhao, K. An, C. Lin, H. Liu, Injectable dextran hydrogels fabricated by metal-free click chemistry for cartilage tissue engineering, Mater. Sci. Eng. C 73 (2017) 21–30.

[14] H. Salimi-Kenari, F. Mollaie, E. Dashtimoghadam, M. Imani, B. Nyström, Effects of chain length of the cross-linking agent on rheological and swelling characteristics of dextran hydrogels, Carbohydr. Polym. 181 (2018) 141–149.

[15] P. Nikpour, H. Salimi-Kenari, F. Fahimipour, S.M. Rabiee, M. Imani, E. Dashtimoghadam, L. Tayebi, Dextran hydrogels incorporated with bioactive glass-ceramic: nanocomposite scaffolds for bone tissue engineering, Carbohydr. Polym. 190 (2018) 281–294.

[16] D. Algul, H. Sipahi, A. Aydin, F. Kelleci, S. Ozdatli, F.G. Yener, Biocompatibility of biomimetic multilayered alginate–chitosan/β-TCP scaffold for osteochondral tissue, Int. J. Biol. Macromol. 79 (2015) 363–369.

[17] S. Bose, S. Tarafder, A. Bandyopadhyay, Effect of chemistry on osteogenesis and angiogenesis towards bone tissue engineering using 3D printed scaffolds, Ann. Biomed. Eng. 45 (1) (2017) 261–272.

[18] K. Noritake, S. Kuroda, M. Nyan, Y. Atsuzawa, M. Uo, K. Ohya, S. Kasugai, Use of a gelatin hydrogel membrane containing β-tricalcium phosphate for guided bone regeneration enhances rapid bone formation, Dent. Mater. J. 33 (5) (2014) 674–680.

[19] S.A. Park, H.-J. Lee, K.-S. Kim, S.J. Lee, J.-T. Lee, S.-Y. Kim, N.-H. Chang, S.-Y. Park, In vivo evaluation of 3D-printed polycaprolactone scaffold implantation combined with β-TCP powder for alveolar bone augmentation in a beagle defect model, Materials 11 (2) (2018) 238.

[20] R. Trombetta, J.A. Inzana, E.M. Schwarz, S.L. Kates, H.A. Awad, 3D printing of calcium phosphate ceramics for bone tissue engineering and drug delivery, Ann. Biomed. Eng. 45 (1) (2017) 23–44.

[21] Y. Wen, S. Xun, M. Haoye, S. Baichuan, C. Peng, L. Xuejian, Z. Kaihong, Y. Xuan, P. Jiang, L. Shibi, 3D printed porous ceramic scaffolds for bone tissue engineering: a review, Biomaterials Science 5 (9) (2017) 1690–1698.

[22] I. Serra, R. Fradique, M. Vallejo, T. Correia, S. Miguel, I. Correia, Production and characterization of chitosan/gelatin/β-TCP scaffolds for improved bone tissue regeneration, Mater. Sci. Eng. C 55 (2015) 592–604.

[23] H.-I. Chang, Y. Wang, Cell responses to surface and architecture of tissue engineering scaffolds, Regenerative Medicine and Tissue Engineering-Cells and Biomaterials, InTech open, 2011.

[24] A.J. Salgado, O.P. Coutinho, R.L. Reis, Bone tissue engineering: state of the art and future trends, Macromol. Biosci. 4 (8) (2004) 743–765.

[25] H.S. Kenari, M. Imani, A. Nodehi, Full factorial design-of-experiments for preparation of crosslinked dextran microspheres, J. Appl. Polym. Sci. 127 (5) (2013) 3712–3724.

[26] H.S. Kenari, Z. Alinejad, M. Imani, A. Nodehi, Effective parameters in determining cross-linked dextran microsphere characteristics: screening by Plackett–Burman design-of-experiments, J. Microencapsul. 30 (6) (2013) 599–611.

[27] H.S. Kenari, M. Imani, E. Dashtimoghadam, A. Maleki, B. Nyström, A. Nodehi, Oscillatory rheometric tracing of dextran crosslinking reaction in aqueous semidilute solutions–effects of formulation on the gelation properties, Polymer 54 (12) (2013) 2999–3007.

[28] A. Tampieri, M. Sandri, E. Landi, G. Celotti, N. Roveri, M. Mattioli-Belmonte, L. Virgili, F. Gabbanelli, G. Biagini, HA/alginate hybrid composites prepared through bio-inspired nucleation, Acta Biomater. 1 (3) (2005) 343–351.

[29] S. Zhou, X. Zheng, X. Yu, J. Wang, J. Weng, X. Li, B. Feng, M. Yin, Hydrogen bonding interaction of poly (D, L-lactide)/hydroxyapatite nanocomposites, Chem. Mater. 19 (2) (2007) 247–253.

[30] M.S. Hasnain, A.K. Nayak, M. Singh, M. Tabish, M.T. Ansari, T.J. Ara, Alginate-based bipolymeric-nanobioceramic composite matrices for sustained drug release, Int. J. Biol. Macromol. 83 (2016) 71–77.

[31] S. Shi, S. Chen, X. Zhang, W. Shen, X. Li, W. Hu, H. Wang, Biomimetic mineralization synthesis of calcium-deficient carbonate-containing hydroxyapatite in a three-dimensional network of bacterial cellulose, Journal of Chemical Technology & Biotechnology: International Research in Process, Environmental & Clean Technology 84 (2) (2009) 285–290.

[32] Y. Wan, Y. Huang, C. Yuan, S. Raman, Y. Zhu, H. Jiang, F. He, C. Gao, Biomimetic synthesis of hydroxyapatite/bacterial cellulose nanocomposites for biomedical applications, Mater. Sci. Eng. C 27 (4) (2007) 855–864.

[33] F.-H. Lin, C.-H. Yao, J.-S. Sun, H.-C. Liu, C.-W. Huang, Biological effects and cytotoxicity of the composite composed by tricalcium phosphate and glutaraldehyde cross-linked gelatin, Biomaterials 19 (10) (1998) 905–917.

[34] D. İmren, M. Gümüşderelioğlu, A. Güner, Synthesis and characterization of dextran hydrogels prepared with chlor-and nitrogen-containing crosslinkers, J. Appl. Polym. Sci. 102 (5) (2006) 4213–4221.

[35] C. Gao, G.Y. Xiong, H.L. Luo, K.J. Ren, Y. Huang, Y.Z. Wan, Dynamic interaction between the growing Ca–P minerals and bacterial cellulose nanofibers during early biomineralization process, Cellulose 17 (2) (2010) 365–373.

[36] W. Fan, L. Zuo, Y. Zhang, Y. Chen, T. Liu, Mechanically strong polyimide/carbon nanotube composite aerogels with controllable porous structure, Compos. Sci. Technol. 156 (2018) 186–191.

[37] Z. Zhang, L. Chen, C. Zhao, Y. Bai, M. Deng, H. Shan, X. Zhuang, X. Chen, X. Jing, Thermo-and pH-responsive HPC-g-AA/AA hydrogels for controlled drug delivery applications, Polymer 52 (3) (2011) 676–682.

[38] A. Shavandi, A.E.-D.A. Bekhit, Z. Sun, A. Ali, M. Gould, A novel squid pen chitosan/hydroxyapatite/β-tricalcium phosphate composite for bone tissue engineering, Mater. Sci. Eng. C 55 (2015) 373–383.

[39] C. Zhu, S. Pongkitwitoon, J. Qiu, S. Thomopoulos, Y. Xia, Design and fabrication of a hierarchically structured scaffold for tendon-to-bone repair, Adv. Mater. 30 (16) (2018) 1707306.

[40] S.M. Bittner, B.T. Smith, L. Diaz-Gomez, C.D. Hudgins, A.J. Melchiorri, D.W. Scott, J.P. Fisher, A.G. Mikos, Fabrication and mechanical characterization of 3D printed vertical uniform and gradient scaffolds for bone and osteochondral tissue engineering, Acta Biomater. 90 (2019) 37–48.

[41] H.R. Lin, Y.J. Yeh, Porous alginate/hydroxyapatite composite scaffolds for bone tissue engineering: preparation, characterization, and in vitro studies, J. Biomed. Mater. Res. B Appl. Biomater. 71 (1) (2004) 52–65.

[42] K. Haraguchi, K. Matsuda, Spontaneous formation of characteristic layered morphologies in porous nanocomposites prepared from nanocomposite hydrogels, Chem. Mater. 17 (5) (2005) 931–934.

[43] F. Beladi, S. Saber-Samandari, S. Saber-Samandari, Cellular compatibility of nanocomposite scaffolds based on hydroxyapatite entrapped in cellulose network for bone repair, Mater. Sci. Eng. C 75 (2017) 385–392.

[44] Y. Bao, J. Ma, Y. Sun, Swelling behaviors of organic/inorganic composites based on various cellulose derivatives and inorganic particles, Carbohydr. Polym. 88 (2) (2012) 589–595.

[45] M.A. Chowdhury, D.J. Hill, A.K. Whittaker, Mass uptake study of the diffusion of water and SBF into poly (2-hydroxyethyl methacrylate-co-tetrahydrofurfuryl methacrylate) containing aspirin or vitamin B12, J. Biomater. Sci. Polym. Ed. 16 (8) (2005) 1047–1061.

[46] Y. Lei, B. Rai, K. Ho, S. Teoh, In vitro degradation of novel bioactive polycaprolactone —20% tricalcium phosphate composite scaffolds for bone engineering, Mater. Sci. Eng. C 27 (2) (2007) 293–298.

[47] M.S. Belluzo, L.F. Medina, A.M. Cortizo, M.S. Cortizo, Ultrasonic compatibilization of polyelectrolyte complex based on polysaccharides for biomedical applications, Ultrason. Sonochem. 30 (2016) 1–8.

[48] F.S. Aggor, E.M. Ahmed, A. El-Aref, M. Asem, Synthesis and characterization of poly (acrylamide-co-acrylic acid) hydrogel containing silver nanoparticles for antimicrobial applications, Journal of American Science 12 (6) (2010).

[49] L. Cai, F. Han, J. Hu, G. Xu, Y. Huang, X. Lin, The effect of the preparation process on the swelling behavior of silk fibroin-polyurethane composite hydrogels using a full factorial experimental design, J. Polym. Eng. 35 (6) (2015) 523–531.

[50] Y. Zhao, T. Tan, T. Kinoshita, Swelling kinetics of poly (aspartic acid)/poly (acrylic acid) semi-interpenetrating polymer network hydrogels in urea solutions, J. Polym. Sci. B Polym. Phys. 48 (6) (2010) 666–671.
[51] M.S. Saveleva, K. Eftekhari, A. Abalymov, T.E.L. Douglas, D. Volodkin, B.V. Parakhonskiy, A.G. Skirtach, Hierarchy of hybrid materials–the place of inorganics-in-organics in it, their composition and applications, Frontiers in Chemistry 7 (2019) 179.
[52] M. Azami, F. Moztarzadeh, M. Tahriri, Preparation, characterization and mechanical properties of controlled porous gelatin/hydroxyapatite nanocomposite through layer solvent casting combined with freeze-drying and lamination techniques, J. Porous. Mater. 17 (3) (2010) 313–320.
[53] A.J.W. Johnson, B.A. Herschler, A review of the mechanical behavior of CaP and CaP/polymer composites for applications in bone replacement and repair, Acta Biomater. 7 (1) (2011) 16–30.
[54] R.Y. Basha, M. Doble, Design of biocomposite materials for bone tissue regeneration, Mater. Sci. Eng. C 57 (2015) 452–463.
[55] E. El-Meliegy, N. Abu-Elsaad, A.M. El-Kady, M.A. Ibrahim, Improvement of physico-chemical properties of dextran-chitosan composite scaffolds by addition of nano-hydroxyapatite, Sci. Rep. 8 (1) (2018), 12180.
[56] D. Algul, A. Gokce, A. Onal, E. Servet, A.I. Dogan Ekici, F.G. Yener, In vitro release and in vivo biocompatibility studies of biomimetic multilayered alginate-chitosan/β-TCP scaffold for osteochondral tissue, J. Biomater. Sci. Polym. Ed. 27 (5) (2016) 431–440.
[57] C. Weinand, I. Pomerantseva, C.M. Neville, R. Gupta, E. Weinberg, I. Madisch, F. Shapiro, H. Abukawa, M.J. Troulis, J.P. Vacanti, Hydrogel-β-TCP scaffolds and stem cells for tissue engineering bone, Bone 38 (4) (2006) 555–563.